Geophysical Journal International

Geophys. J. Int. (2011) **185,** 676–692 doi: 10.1111/j.1365-246X.2011.04973.x

Source model for the 1997 Zirkuh earthquake ($M_W = 7.2$) in Iran derived from JERS and ERS InSAR observations

Henriette Sudhaus* and Sigurjón Jónsson†

ETH Zurich, Institute of Geophysics, Sonneggstr. 5, 8092 *Zurich, Switzerland. E-mail: hsudhaus@gfz-potsdam.de*

Accepted 2011 January 27. Received 2010 October 20; in original form 2010 January 13

SUMMARY

We present the first detailed source model of the 1997 M7.2 Zirkuh earthquake that ruptured the entire Abiz fault in East Iran producing a 125 km long, bended and segmented fault trace. Using SAR data from the ERS and JERS-1 satellites we first determined a multisegment fault model for this predominately strike-slip earthquake by estimating fault-segment dip, slip, and rake values using an evolutionary optimization algorithm. We then inverted the InSAR data for variable slip and rake in more detail along the multisegment fault plane. We complement our optimization with importance sampling of the model parameter space to ensure that the derived optimum model has a high likelihood, to detect correlations or trade-offs between model parameters, and to image the model resolution. Our results are in an agreement with field observations showing that this predominantly strike-slip earthquake had a clear change in style of faulting along its rupture. In the north we find that thrust faulting on a westerly dipping fault is accompanied with the strike-slip that changes to thrust faulting on an eastward dipping fault plane in the south. The centre part of the fault is vertical and has almost pure dextral strike-slip. The heterogeneous fault slip distribution shows two regions of low slip near significant fault step-overs of the Abiz fault and therefore these fault complexities appear to reduce the fault slip. Furthermore, shallow fault slip is generally reduced with respect to slip at depth. This shallow slip deficit varies along the Zirkuh fault from a small deficit in the North to a much larger deficit along the central part of the fault, a variation that is possibly related to different interseismic repose times.

Key words: Radar interferometry; Earthquake source observations; Asia.

1 INTRODUCTION

On 1997 May 10 the Zirkuh earthquake ruptured the entire Abiz Fault, which at 125 km is the longest fault rupture ever observed in Iran (Fig. 1). The settlements near the fault suffered severe structural damage in the earthquake, around 1600 people were killed and about 50 000 were left homeless (Berberian *et al.* 1999). This region is the area with the highest seismic hazard in eastern Iran (Grünthal *et al.* 1999). The northern part of the Abiz Fault had already been the source of three $M > 6$ earthquakes within the same century (Berberian *et al.* 1999). The Zirkuh earthquake ruptured the segmented and curved Abiz fault with right-lateral surface displacements of up to 2 m and thrust components that locally reached tens of centimetres, according to measurements by Berberian *et al.* (1999). The complex nature of the Zirkuh surface rupture is evident from the results of detailed mapping of the fault trace and dense measurements of the amount of slip along the fault. In contrast, the characteristics of the earthquake at depth are poorly known. No local seismic recordings or coseismic GPS data exist of the Zirkuh earthquake, because no such networks were in place in the region at the time of the earthquake.

The potential of utilizing InSAR data to learn more about the rupture process of the Zirkuh earthquake was recognized a few years after the earthquake. The arid climate and limited farming in the semi-desert in eastern Iran do suggest good conditions for InSAR and already in 2000 and 2003 coseismic interferograms were presented at geoscientific conferences (Fielding *et al.* 2000; Lohman & Simons 2001; Peyret *et al.* 2004). However, attempts to image the Zirkuh source using these InSAR data were abandoned, because of the earthquake's size and complexity, together with the rather limited InSAR data coverage in eastern Iran (E. Fielding, personal communication, 2008).

In this study, we combine InSAR data from the European ERS C-band ($\lambda = 5.6$ cm) and the Japanese JERS-1 L-band ($\lambda = 23.5$ cm) radar satellites to measure the coseismic surface deformation. By combining these data we benefit from the relatively low data

*Now at: Helmholtz Centre Potsdam GFZ, Helmholtzstr.7 H7/320, 14467 Potsdam, Germany.
†Now at: King Abdullah University of Science and Technology (KAUST), Thuwal 23955-6900, Saudi Arabia.

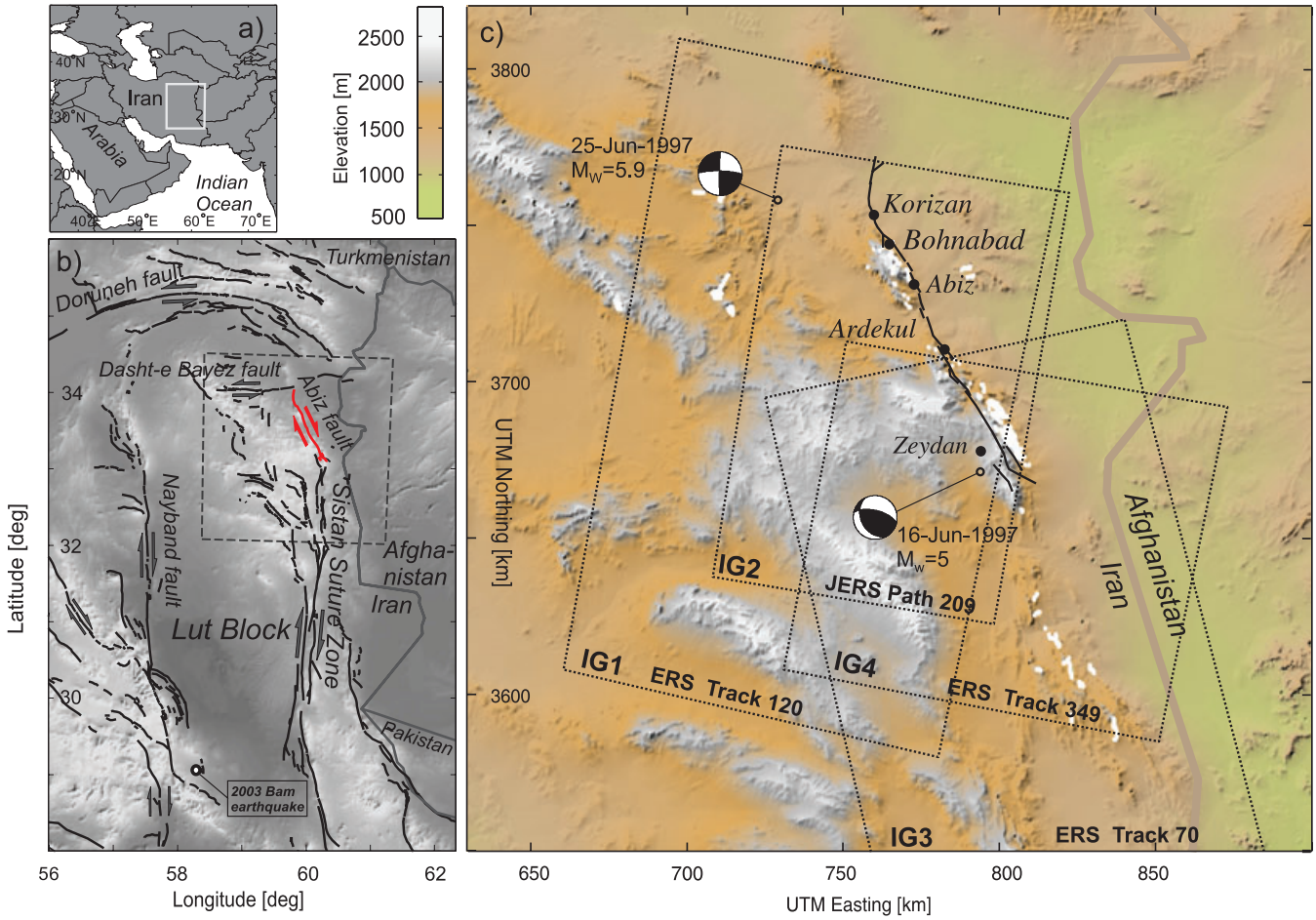

Figure 1. Tectonics and elevation of East Iran. (a) Location of East Iran and (b) the major faults and fault systems around the Lut Block after Walker & Khatib (2006) with the Abiz fault (red) and the coverage of Fig. 1(c). (c) Topographic map of eastern Iran showing the surface rupture trace (thick black line) of the Zirkuh Earthquake after Berberian *et al.* (1999), towns affected by the Zirkuh earthquake and the locations of two $M > 5$ aftershocks with their focal mechanisms (Farahbod *et al.* 2003). The area covered by the interferograms IG1-IG4 (Table 1) is marked with thin black rectangles. White spots in the elevation map result from gaps in the SRTM (Space Shuttle Radar Mission) elevation model.

errors of C-band interferograms on one hand and from the ability of L-band data to measure large surface displacements near the fault as well as their resistance to temporal decorrelation on the other hand.

2 THE ZIRKUH EARTHQUAKE

The Zirkuh earthquake ruptured the NNW–SSE striking Abiz Fault that forms the northern tip of the Sistan Suture Zone in eastern Iran. The Sistan Suture Zone developed during the Eocene when the Lut and the Afghan blocks collided, but earlier they were parts of the same landmass that then had been separated through rifting processes around 140 Myr BP (Berberian & King 1981; Berberian *et al.* 1999). The Sistan Suture Zone is now a major active zone (Walker & Khatib 2006), accommodating right-lateral movements between the more rigid crust to the east (Afghanistan and southwest Pakistan) and the NS-oriented crustal shortening taking place west of the suture in Iran's north and south (Berberian *et al.* 1999; Vernant *et al.* 2004).

Berberian *et al.* (1999) provide detailed information about the surface fault trace based on field observations made shortly after the earthquake. The mapped fault trace and the surface offset measurements point to changes of the rupture mechanism along the fault which motivated their in-depth moment-tensor analysis based on teleseismic records. In their study, the waveforms were analysed as if resulting from four subsequent events, each representing the mechanism for a certain portion of the long rupture. The corresponding moment tensors vary from almost pure strike-slip in the north to mechanisms dominated by thrust faulting in the south (Berberian *et al.* 1999).

No near-field seismic observations of the Zirkuh earthquake exist. The Iranian seismic network was under construction in 1997, with its functional part near Teheran, more than 600 km away from the epicentre. Other seismic stations, for example of the Global Seismic Network (GSN), are located even farther away. A temporary seismic network was installed some days after the Zirkuh earthquake in the epicentral area and 20 stations recorded aftershocks for several months (Farahbod *et al.* 2003). However, the hypocentre distribution of 219 relocated aftershocks with magnitudes above 2.5 is not very focussed and therefore does not provide information about the fault plane at depth (Farahbod *et al.* 2003).

3 ERS AND JERS-1 SAR DATA

The Abiz fault is well covered by two parallel descending tracks and one ascending track of the ERS satellites. However, the number

Table 1. Processed ERS and JERS-1 interferograms. The first four interferograms were used in the model estimation. ERS data were provided by the European Space Agency (ESA) and JERS-1 data were ordered at the Remote Sensing Technology Center of Japan (RESTEC).

No.	Sensor	Pass	Track	Frame	Master	Slave	$B_\perp$	B_T
IG1	ERS-2	desc.	120	2925,2943	96/04/03	99/03/24	136	2 yr 355 d
IG2	JERS-1	desc.	209	244,245	94/11/15	97/07/10	1060	3 yr 25 d
IG3	ERS-1/2	asc.	70	657	96/03/30	98/08/22	21	2 yr 145 d
IG4	ERS-2	desc.	349	2943	96/05/24	98/09/11	25	2 yr 110 d
5	ERS-1/2	desc.	349	2925,2943	92/05/26	99/06/18	139	7 yr 23 d
6	ERS-1/2	desc.	349	2925,2943	92/11/17	99/06/18	182	7 yr 152 d
7	ERS-1/2	desc.	77	2943	96/03/30	98/03/23	106	2 yr 146 d
8	ERS-2	desc.	77	2943	96/05/05	99/05/30	34	3 yr 25 d
9	ERS-1/2	asc.	299	657	96/05/19	98/09/07	66	2 yr 111 d
10	ERS-1/2	asc.	299	657	96/05/19	97/06/09	105	2 yr 21 d

$B_\perp$, perpendicular baseline between the orbits in metres. B_T, temporal baseline between acquisitions in years and days.

of ERS SAR scenes acquired over eastern Iran is limited and the coseismic SAR interferograms we were able to form all span at least 2 yr (Table 1). We processed the SAR data and calculated interferograms with the GAMMA processing software (Werner *et al.* 2000) using reestimated satellite orbits (Scharoo *et al.* 1998). The topography-related phase was removed from the interferograms using the Shuttle Radar Topography Mission (SRTM; Farr *et al.* 2007) 3 arcsec (∼90 m resolution) digital elevation model (DEM). The rather long timespan of the interferograms strongly influences the interferometric phase coherence and we therefore enhanced the signal-to-noise-ratio by multilooking (4 × 4) the interferograms, resulting in a ground resolution close to the resolution of the DEM. We then projected the DEM and the interferograms to cartesian UTM coordinates (UTM zone 40S) with a pixel size of 76 m in the east direction and 96 m in the north direction. Finally, we applied an adaptive power spectral filter to the geocoded interferograms (Goldstein & Werner 1998) to further suppress data noise.

The JERS-1 satellite of the Japan Aerospace Exploration Agency (JAXA) was still operating at the time of the Zirkuh earthquake. We obtained JERS-1 data covering the fault acquired from a descending track (JERS-1 Track/Path 209) before and after the Zirkuh earthquake. Processing of JERS-1 interferograms is similar to the ERS processing, except no precise orbital estimations for JERS-1 exist. Therefore, we had to remove a significant residual orbital phase ramp manually from the JERS-1 interferogram as the coseismic surface deformation extends over the major part of the interferogram.

From the processed data (Table 1) we selected four interferograms, two descending and one ascending ERS interferograms (C-band, $\lambda = 5.6$ cm), and the descending JERS-1 interferogram (L-band, $\lambda = 23.5$ cm). The interferograms from descending passes cover the entire fault rupture, whereas the ascending interferogram covers only the southern half of the fault (Fig. 2).

The coseismic deformation expressed in the interferograms covers a large area, extending to more than 60 km away from the surface fault trace and exceeding the east–west extent of the JERS-1 as well as of the ERS interferograms (Fig. 2). The cycles of interferometric phase shifts, called fringes, show a very complex pattern as anticipated from such a large earthquake. West of the fault trace we observe in the ERS descending interferograms a range increase, or movement of the ground away from the satellite, of up to seven fringes in the north and 11 fringes in the south, which corresponds to 20 and 30 cm of negative line-of-sight (LOS) surface displacement, respectively. Closer to the fault the fringe rate increases and in most cases the interferometric phase is completely decorrelated near the fault trace. Therefore, the maximum LOS displacement is likely to be considerably larger than what we are able to observe in the ERS interferograms. In the L-band JERS-1 interferogram (IG2) the coherent interferometric phase draws far closer to the fault. The largest LOS displacement on the western side of the fault is found near to the southern end of the rupture amounting to about −60 cm. The JERS-1 LOS displacements are not directly comparable with those of ERS, because of the different look angle of the sensors. The incidence angle of JERS-1 is about 15° larger and the observed LOS displacement of the surface has therefore a larger horizontal contribution, which is likely the dominant surface displacement caused by this predominantly strike-slip earthquake.

Along the eastern side of the fault we observe in the descending interferograms positive and negative LOS displacements. In IG1 (ERS interferogram), the LOS displacements reach −15 cm in the north, 20 km towards the south it increases to about 8 cm before decreasing again to −15 cm after another 15 km. Further south we measure again increasing LOS displacements that reach 30 cm. In general, the LOS displacements in the northern part of the rupture are smaller than in the south.

The ascending ERS interferogram (IG3) covers only the southern part of the fault. The largest LOS displacement we observe here is around −30 cm on the western side of the fault, whereas the coherent area east of the fault shows only a few fringes. The ascending LOS vector is oriented almost orthogonal to the fault trace and therefore the ascending LOS observations are less sensitive to horizontal, fault parallel displacements than the LOS measurements from descending tracks. Hence, the ascending fringe pattern points to significant vertical displacements close to the southern tip of the fault.

The interferograms also span two of the largest aftershocks: the 1997 June 16 thrust earthquake ($M_W = 5$) and the 1997 June 25 strike-slip earthquake ($M_W = 6.0$) (Figs 1 and 2). The thrust earthquake occurred close to the southern end of the Zirkuh rupture and its deformation signal is not detectable within the dominant signal of the Zirkuh mainshock. The second event caused visible surface deformation around 40 km west of the northern end of the fault, forming a small round pattern in one of the interferograms (Fig. 2a). At this point, the ground moved towards the radar and therefore in the opposite sense of displacement to the surrounding area.

Temporal decorrelation, strong topographic relief, loss of coherence due to earthquake-associated landsliding and high fringe rate all limit the quality of the interferograms close to the fault rupture. The 2- to 3-yr C-band interferograms exhibit a strong local coherence degradation where large alluvial fans have formed in

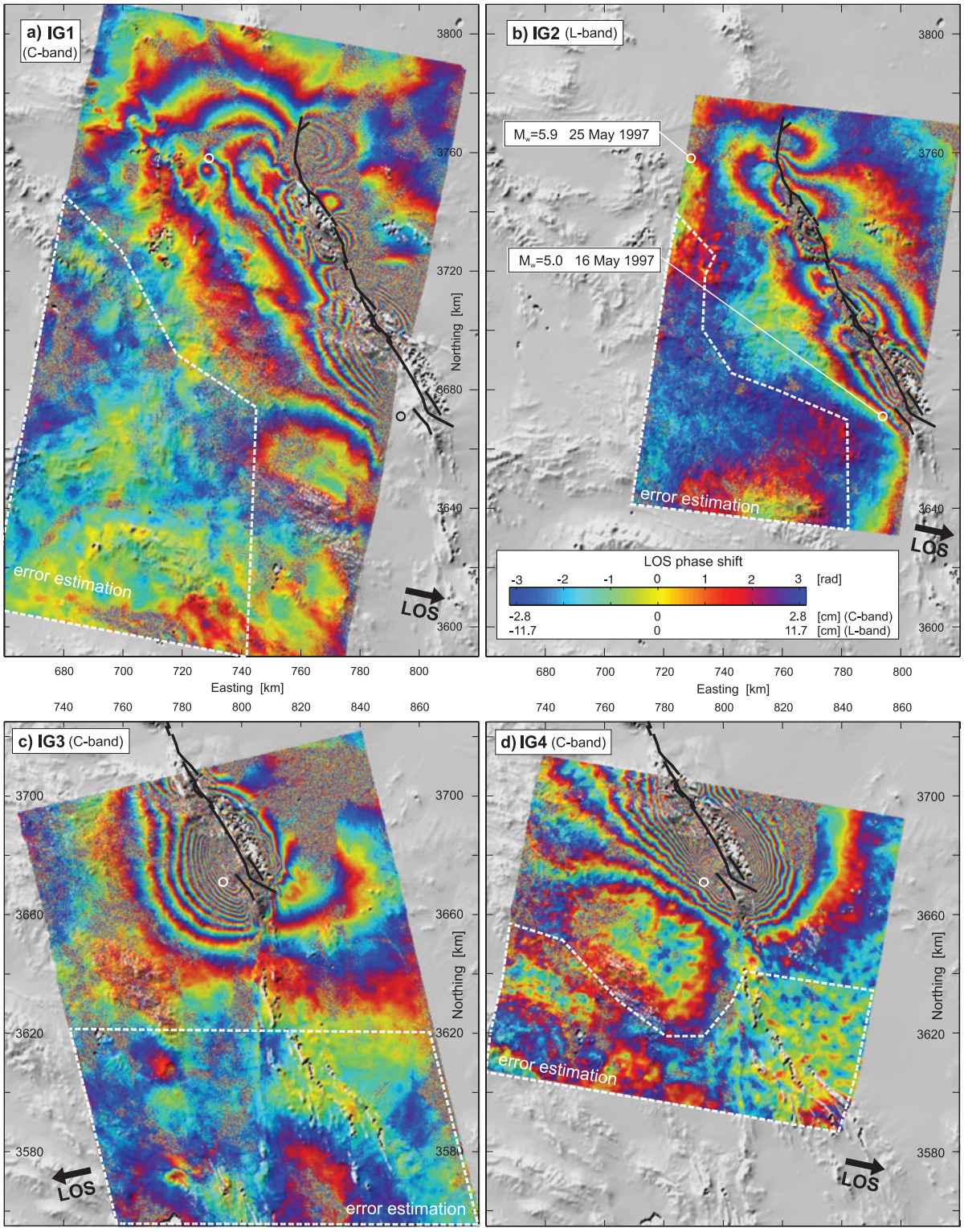

Figure 2. Interferograms from ERS-1/2 (C-band) and JERS-1 (L-band) satellite data (Table 1) with indicated line-of-sight direction (arrows) in foreground of shaded topography in UTM coordinates (UTM zone 40S). Two aftershocks with $M > 5$ are marked by white circles and outlined with white dashed lines are areas where data errors were estimated.

the mountainous foreland. The 3-yr L-band interferogram, on the other hand, captures clearly the LOS surface displacement in these places. Many of the alluvial fans have formed on the east side of the fault escarpment and the JERS-1 interferogram therefore provides important near-field information.

In addition, the strong topographic relief in eastern Iran with elevations ranging from 500 to 2800 m (Fig. 1) causes many layovers in the interferograms at slopes facing towards the satellite look direction and shadow zones on the far side. For the JERS-1 sensor layovers are less common than for ERS

whereas shadows are more common, due to its larger incidence angle.

We unwrapped the interferograms using the statistical-cost network-flow unwrapping algorithm *snaphu* by Chen & Zebker (2001) (see Supporting Information). Interferogram IG1 suffers from noise northeast of the fault that made the phase unwrapping difficult in this part of the interferogram. Therefore, in a separate step, we multilooked IG1 by 30 pixels in the range and azimuth directions to increase the signal-to-noise-ratio. We then unwrapped the resampled interferogram in this area and used the result to improve the coverage of the unwrapped phase in IG1.

4 ESTIMATION OF INSAR DATA ERRORS

When using multiple interferograms in modelling calculations it is important to assess the error of each data set to weight the observations appropriately. The contributions to the total InSAR data error from error sources on the ground and along the wave path are distinctive for each interferogram (Hanssen 2001) and we therefore empirically estimate the data error in the interferograms. We describe the error structure with auto-covariance functions to account for the correlation of the InSAR data errors.

Atmospheric phase delays are clearly visible in the nondeforming parts of the four interferograms. This noise is most pronounced in IG4 (Fig. 2d) where the undulation of phase shifts reaches amplitude of almost one phase cycle and has a spatial wavelength of about 10 km. Such phase undulations appear also in IG1 (Fig. 2a), but with a larger wavelength (∼15 km) and weaker amplitude. In IG1, we also observe an imprint of elevation dependent phase shift, which shows up even clearer in IG2 and IG3, because they are less affected by noise from the turbulent atmosphere. The apparent atmospheric noise in the L-band interferogram IG2 contains also spatial wavelengths that are significantly longer than 15 km (Fig. 2b).

For the empirical error estimation we use a geostatistical approach and form sample semi-variograms and covariograms in areas of the interferograms that are not influenced by the coseismic deformation (Fig. 2). By using this approach we generalize the data error across areas with spatially varying phase coherence and for areas showing topography-related atmospheric phase shifts. Moreover, we let the estimated error statistics represent the data error of the entire interferograms, that is we implicitly assume stationarity of the data errors. Even if these assumptions may not be entirely accurate, including partially correct data error characteristics will improve the modelling with respect to neglecting correlated data errors altogether (Knospe & Jónsson 2009). The interferometric phase in the outlined areas in Fig. 2 shows only a weak or no anisotropic structure (Knospe & Jónsson 2009), so that the error statistics can be characterized by 1-D auto-covariance functions depending only on the distance.

We generate the sample semi-variograms and co-variograms for each data set by calculating the variance and covariance of point pairs that we randomly sample in nondeforming parts of the interferograms (Sudhaus & Jónsson 2009). To these covariograms we then fit covariance functions $\mathrm{cov}(h)$ using a positive-definite function type of the form $\mathrm{cov}(h) = b\exp(-h/a)$ with $[a, b] \in \mathbb{R}^+$. The covariance functions are defined for distances larger than zero and we extend them to zero with the data error variance, estimated from the semi-variograms (Fig. 3, Table 2).

For the C-band interferograms we find that the relative values of error variance and covariance reflect well the interferogram qualities as inspected by eye. The data error variance is largest in IG4 and data error of IG1, IG3 and IG4 is correlated up to 20 km. The error estimation for the L-band interferogram IG2 is complicated by the fact that only a small area in the interferogram can be used for the error estimation. Because robust statistical estimates can only be made for spatial wavelengths well within the smallest extension of the estimation area (Chilés & Delfiner 1999) and the apparent atmospheric noise in IG2 clearly contains periods greater than the area we used in the data error estimation (Fig. 2), the IG2 data variance estimation as well as the covariogram may be biased. For simplification, we used the same function type to fit the IG2 covariogram as we used for IG1, IG3 and IG4 and tolerate the mismatch in the shape of covariogram and covariance function. The data variance and covariance of IG2 are much larger than the values estimated for the C-band interferograms and the IG2 data weights assigned in the modelling are accordingly small. We assume that the effect of a biased error estimation for IG2 in the modelling is negligible. The variance–covariance functions give descriptions of the data error structure that is continuous with distance and from these functions we derive the variance–covariance matrix Σ of the data set that we use in the fault modelling.

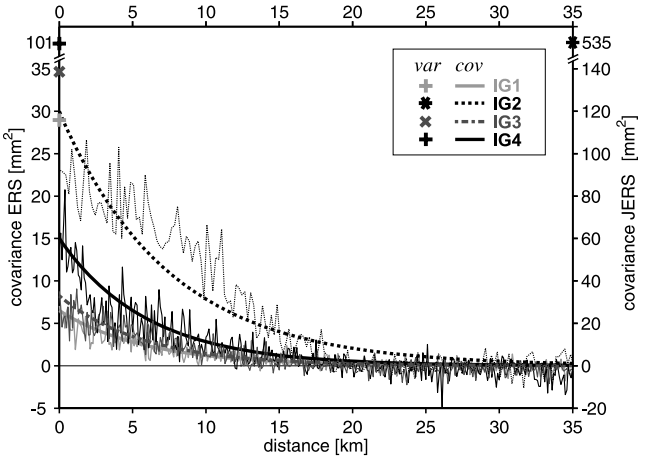

Figure 3. Data error auto-covariograms (thin lines) and fitted auto-covariance functions (thick lines) for IG1-4 (Fig. 1, Table 2) with two different scales for the ERS interferograms (left ordinate) and the JERS-1 interferogram (right ordinate). The estimated data error auto-variances are marked at the corresponding ordinates to the left and right.

Table 2. Data error variance and the parameters a and b of the data error auto-covariance functions $\mathrm{cov}(h) = b\exp(-h/a)$ for IG1-4 plotted in Fig. 3.

	Variance (mm^2)	Covariance b (mm^2)	a (km)
IG1	29	6.5	5.6
IG2	535	120	7.5
IG3	35	8.3	5.7
IG4	101	15	6

5 FAULT MODELLING

A complex fault model with several segments is needed to represent the curved fault trace and the variability of slip along the fault that was observed in the field (Berberian *et al.* 1999). For each

segment we estimate the segment slip and rake, as well as the dip and depth extension of the segment. We use an evolutionary algorithm (Monelli & Mai 2008) to explore the model space in search for the model that minimizes the data misfit $\|e\|$ between the predicted data $\mathbf{d}_{\rm pred}$ and the observed data $\mathbf{d}_{\rm obs}$:

$$\|e\| = \sqrt{(\mathbf{R}(\mathbf{d}_{obs} - \mathbf{d}_{pred}))^{\mathbf{T}}\mathbf{R}(\mathbf{d}_{obs} - \mathbf{d}_{pred})}, \quad (1)$$

with a data weighting matrix $\mathbf{R}$ that we derive from the data variance–covariance matrix Σ.

In this section we describe the data weighting and the optimization set-up. We also introduce the importance sampling (Sambridge & Mosegaard 2002; Monelli *et al.* 2009) we adapt in our study to monitor the performance of the optimization and to estimate the model parameter uncertainties. From our first fault model with uniform fault slip on each segment, we proceed to an optimization set-up that uses correlation constraints between dip values on neighbouring fault segments to obtain physically more plausible fault-dip variations along the fault and to stabilize the model calculations. Finally, we keep the most likely fault geometry fixed, subdivide the segments in many subfaults, and estimate variable fault slip and rake across the segments.

5.1 Data subsampling and weighting

To facilitate the modelling calculations, we need to reduce the number of the data points, which in total for the unwrapped data is more than 4.5 million. We use a quadtree algorithm (Jónsson *et al.* 2002) to irregularly subsample the data. This method results in only a few data points where the interferogram surface displacement pattern is smooth, but retains denser sampling in other parts of the image. We can write the quadtree subsampling procedure as a linear operation, where an operator $\mathbf{A}$ relates the full data vector $\mathbf{d}_{\rm c}$ to a subsampled data vector $\mathbf{d}$:

$$\mathbf{d} = \mathbf{A}\mathbf{d}_{\rm c}. \quad (2)$$

For the N_i pixels of $\mathbf{d}_{\rm c}$, that are averaged to d_i, the corresponding N_i values in the ith row of $\mathbf{A}$ are equal to $1/N_i$, but zero elsewhere. The subsampled data set $\mathbf{d}$ consists of about 5800 data points, which is less than 2 per cent of the full data vector $\mathbf{d}_{\rm c}$.

The empirical error statistics show significant differences in the data quality between the four interferograms (Section 4). We account for these differences in the modelling through the weighting matrix $\mathbf{R}$ (eq. 1), which is derived from the data error variance–covariance matrix Σ of the full resolution data. The full variance–covariance matrix is propagated using the subsampling operator $\mathbf{A}$ (eq. 2) to adapt Σ to the subsampled data set as used in the modelling:

$$[\mathbf{A}\Sigma\mathbf{A}^{\mathbf{T}}]^{-1} = \mathbf{R}^{\mathbf{T}}\mathbf{R}. \quad (3)$$

In practice, we calculate one value $[\mathbf{A}\Sigma\mathbf{A}^{\mathbf{T}}]_{i,j}$ at a time from subsets $\mathbf{C}_{N_i \times N_j}$ of Σ. The subsets $\mathbf{C}_{N_i \times N_j}$ are the covariance values corresponding to the pixels combined to the data points d_i and d_j through quadtree subsampling whereas N_i and N_j are the numbers of pixels averaged in these quadtree squares:

$$[\mathbf{A}\Sigma\mathbf{A}^{\mathbf{T}}]_{i,j} = \frac{1}{N_i N_j}\sum_{k=1}^{N_i}\sum_{l=1}^{N_j} C_{kl}. \quad (4)$$

In this way, the relative weight of a data point reflects the variance of the interferogram (high variance lowers the weight), the power of correlated data error (high correlation lowers the weight), and the number of pixels combined in the quadtree square (many pixels increase the weight).

In addition to the heterogeneous data quality, the data coverage of the ground varies from one area to another around the fault. Some areas are covered by only one interferogram and other areas by all four data sets (Figs 1 and 2). Overlapping LOS observations are generally linearly dependent and if we ignore the linear dependence of these data points they will gain artificially high weights and therefore importance in the modelling. Therefore, we consider the correlation between data points from different interferograms with an additional weight factor.

The end-member cases of overlapping observations are measurements from two orthogonal look directions, which are then linearly independent, and two measurements from exactly the same point of view, which can be regarded as repeated measurements of the same surface deformation signal. In the latter case the variance of the mean value is $\mathrm{var}((X+Y)/2) = (\mathrm{var}(X) + \mathrm{var}(Y))/4$. The corresponding weight factor is $\sqrt{2/\mathrm{var}(X)}$ assuming $\mathrm{var}(X) = \mathrm{var}(Y)$, which is less than the weight of two independent points: $2/\sqrt{\mathrm{var}(X)}$.

In our study on the Zirkuh earthquake, neither of the two end-member cases is realized, that is we neither have completely independent measurements nor can we explicitly calculate the mean of the measurements. Interferograms IG1 and IG4 are from two different descending ERS tracks and have therefore only slightly different incidence angles, which differ approximately by 15° from the descending JERS incidence angle in interferogram IG2. The largest incidence angle difference is between the ascending data IG2 and the JERS interferogram, or about 60°. To reflect the degree of linear dependence between the observations, we adapt weights that we determine using the scalar product of the different LOS vectors (for details, see Appendix). The combined weight of data points of the same location on the ground from similar look directions will then be close to the weight of the average value, whereas the combined weight of two points that spatially overlap but have very different LOS vectors will be similar to weights of two independent data points.

5.2 Optimization set-up and importance sampling

We model the Zirkuh rupture as a chain of 17 planar fault segments in an elastic half-space (Okada 1985), located such that they follow the mapped fault surface trace reported by Berberian *et al.* (1999) (Fig. 1), and search for the optimal fault dip, fault width, right-lateral strike-slip and dip-slip of each segment.

This fault model is complemented by two dislocations representing the M_W 5 and M_W 6 aftershocks that occurred close to the main rupture on 1997 June 16 and 25 and within the time span of the interferograms. Although we do not attempt to constrain the mechanisms of these aftershocks, we account for them by fixing their locations, fault dimensions and fault orientations aided by their Global CMT solutions (Dziewonski *et al.* 1981) and estimate only their depth and average slip. Here, the fault dimensions, fault length and fault width, are deduced using the scaling relationship with the moment magnitude after Mai & Beroza (2000). For the M_W 5 thrust, earthquake we assume a 3 km × 3 km fault and for the M_W 6 strike-slip earthquake a fault length of 17 km and a fault width of 11 km. In total, the number of free fault model parameters that we estimate is 68 for the Zirkuh fault and 6 for the two aftershocks.

Beside the earthquake fault model parameters, we also estimate a bilinear planar surface for each interferogram to account for possible orbital errors. In the case of the JERS data we estimate a

quadratic surface instead of a plane, because of the poor JERS orbit information and difficulties in flattening the interferogram as we described in Section 3.

We start the non-linear optimization assuming uniform slip on all fault segments. The large number of data points (∼5800) and the large number of model parameters (74 fault model parameters and 15 orbital ramp parameters) make the optimization challenging. Therefore, we use an evolutionary algorithm (Smith *et al.* 1992; Beyer 2001) with a strong exploration component to model the Zirkuh earthquake. The strength of evolutionary algorithms is that they explore the model space in several places at the same time (Gershenfeld 1999) which is here of high relevance, because most of fault model parameters in our problem are only constrained by a small fraction of the data points. As a result, the optimization reaches different stages of fit. First, the interferogram ambiguity parameters converge, then the fault model parameters of prominent fault segments and so on.

We let the evolutionary algorithm begin with a random set of 200 starting models as the first parent population, from which 800 new models are created by randomly recombining the parental model parameters. These new models (or offsprings) are then altered through random changes in the parameter values given a chosen standard deviation, a procedure that has been called mutation. We implement the model parameter mutation through a standard deviation that we define as a percentage of the corresponding model parameter range, starting with 5 per cent. For each offspring model the model misfit is computed (eq. 1) and we then select from the offsprings the 200 best performing models as the new parental population of the next model generation. The optimization we implemented has four subsequent stages with varying optimization settings. At the first stage, the cycle of recombination, mutation and selection is repeated for 15 model generations (Fig. 4a). At the end of stage 1, the model space has been explored widely and several regions of low misfit have been identified, enabled by the high mutation rate. At the following stage 2 of the optimization with 15 model generations, we decrease the variance of the fault model parameters from a standard deviation of 5 to 2 per cent to enable denser sampling of these low-cost regions. At the same time, we reduce the selection pressure by doubling the number of parents to 400 that are recombined to 900 offspring models. By weakening the selection in this way, we focus a bit less on the better models, but keep exploring other locations of low misfit in the model space. For 15 subsequent generations at stage 3, we aim for a stronger convergence and therefore decrease the mutation rate further to only 1 per cent. Finally, in the last optimization stage with 70 generations, we increase the selection pressure again by reducing the parent population to 200 parents and the number of offsprings to 800 while keeping the model parameter standard deviation at 1 per cent (Fig. 4). This optimization set-up requires several days of computation time on a four-processor workstation.

To ensure that we find models that have a high likelihood in the optimization we apply importance sampling (Sambridge & Mosegaard 2002; Tarantola 2005). Importance sampling is a constrained random walk through the model space so that the distribution of visited models reflects their likelihood. Such a walk starts at a randomly chosen model $\mathbf{m}_0$ from which another model is randomly picked in a distance given by an arbitrary standard deviation of the model parameters that we define as above as the percentage of the defined model parameter limits. $\mathbf{m}_1$ is sampled under the condition that either the misfit of the starting model $\|e(\mathbf{m}_0)\|$ is higher than $\|e(\mathbf{m}_1)\|$ or that the performance of $\mathbf{m}_1$ is only slightly worse than the one of $\mathbf{m}_0$. The model likelihood is $L(\mathbf{m}) = C\exp(-1/2\cdot\|e(\mathbf{m})\|^2)$ assuming a Gaussian distribution of the model parameter uncertainties. The argument 'slightly worse' is also randomized and usually defined as $L(\mathbf{m}_1)/L(\mathbf{m}_0) > r$, an equally distributed random number with $r \in [0\ 1]$. An accepted model $\mathbf{m}_1$ is then the point from which a new model is drawn and in case of a rejection $\mathbf{m}_0$ remains the current point. In this way, models with a good performance get sampled more often than other models. It is required, however, that the model

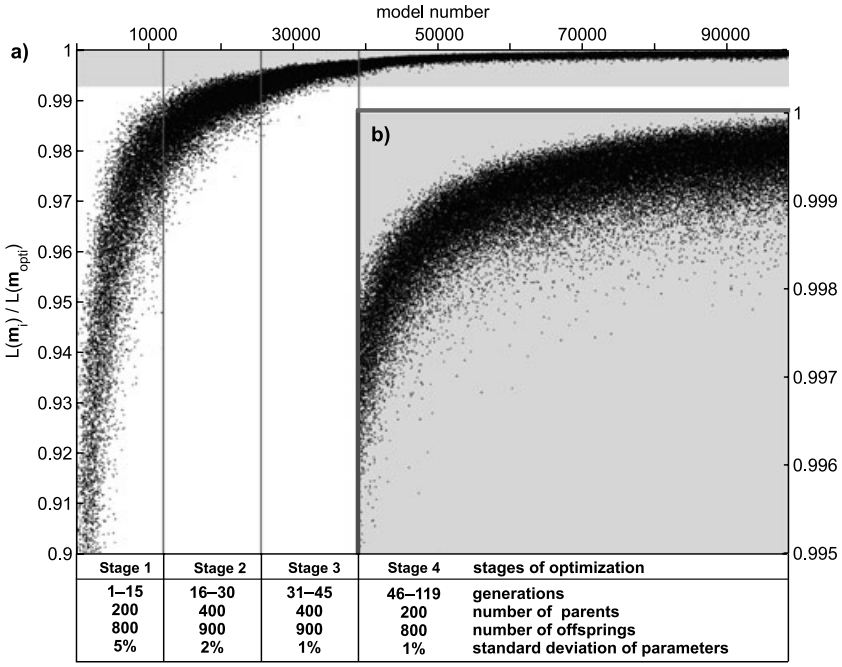

Figure 4. Ratios of the model likelihoods $L(\mathbf{m}_i)/L(\mathbf{m}_{opti})$ for a) the models $\mathbf{m}_i$ visited in the progressing optimization with respect to the optimum model $\mathbf{m}_{opti}$ and b) for the last stage of the optimization at a different scale. Changes of parameters in the four stages of the optimization are indicated with vertical lines and the values of the variable parameters (number of parents, number of offsprings per generation and parameter standard deviation) are given.

cost function along the random walk is uncorrelated. Therefore, we calculate the correlation length of the sampled model costs and, if necessary, decimate the sample series to realize uncorrelated model samples.

We adapt importance sampling to our Zirkuh problem. We choose a standard deviation for the model parameters, marking the step size during the random walk, and a range of r, the selective component, enabling an efficient random walk that accepts every third model (Tarantola 2005). The step size during the random walk needs to be large enough such that the model space can be sufficiently sampled. Choosing a step size that is too large will lead to frequent rejections of picked models, which can seriously hamper the progress of the random walk and is time consuming. Similarly, step sizes that are too small lead to strongly correlated models along the random walk and many models will be lost in the decimation of the model series afterwards. We also reduce the range of r from formerly $r \in [0\ 1]$ significantly to $r \in [0.993\ 1]$. The reason is a relatively weak relation between the model misfit $\|e(\mathbf{m})\|$ and changes in one fault parameter of a certain fault segment, because the fault model parameters are usually controlled by only a small fraction of the data, which is also the reason for the exhaustive optimization. We illustrate this reasoning in Fig. 4 and plot the likelihood ratios of the models visited in the optimization $L(\mathbf{m}_i)$ and the optimum model $L(\mathbf{m}_{\text{opti}})$. Obviously, soon after the start of the optimization, within the first 30 generations of the evolutionary algorithm, the ratios $L(\mathbf{m}_i)/L(\mathbf{m}_{\text{opti}})$ are well within 0.9 and 1. Importance sampling with $r \in [0\ 1]$ would be 'blind' for the difference between the models, so that every picked model would be accepted. With $r \in [0.993\ 1]$ we confine the region where the importance sampling takes place (Fig. 4). On the other hand, more tight ranges on r could cause the random walk to get stuck in a local low of the misfit space. With a standard deviation of 5 per cent and $r \in [0.993\ 1]$, we efficiently sample the model space and obtain stable model parameter distributions for several independent samplings. Since the optimization and the importance sampling are independent from each other, we can use the latter to ensure that the optimization is converging to a region of a global low in the model misfit space or change the optimization settings if it does not.

5.3 Multisegment model of the Zirkuh earthquake

Our estimated multisegment model of the Zirkuh earthquake has right-lateral strike-slip that reaches 2 m near the town Korizan (Figs 5a and b), and around 1.5 m near the town Bohnabad. In the central part of the fault the horizontal displacement varies between 1 m and 1.5 m of right-lateral strike-slip and comes close

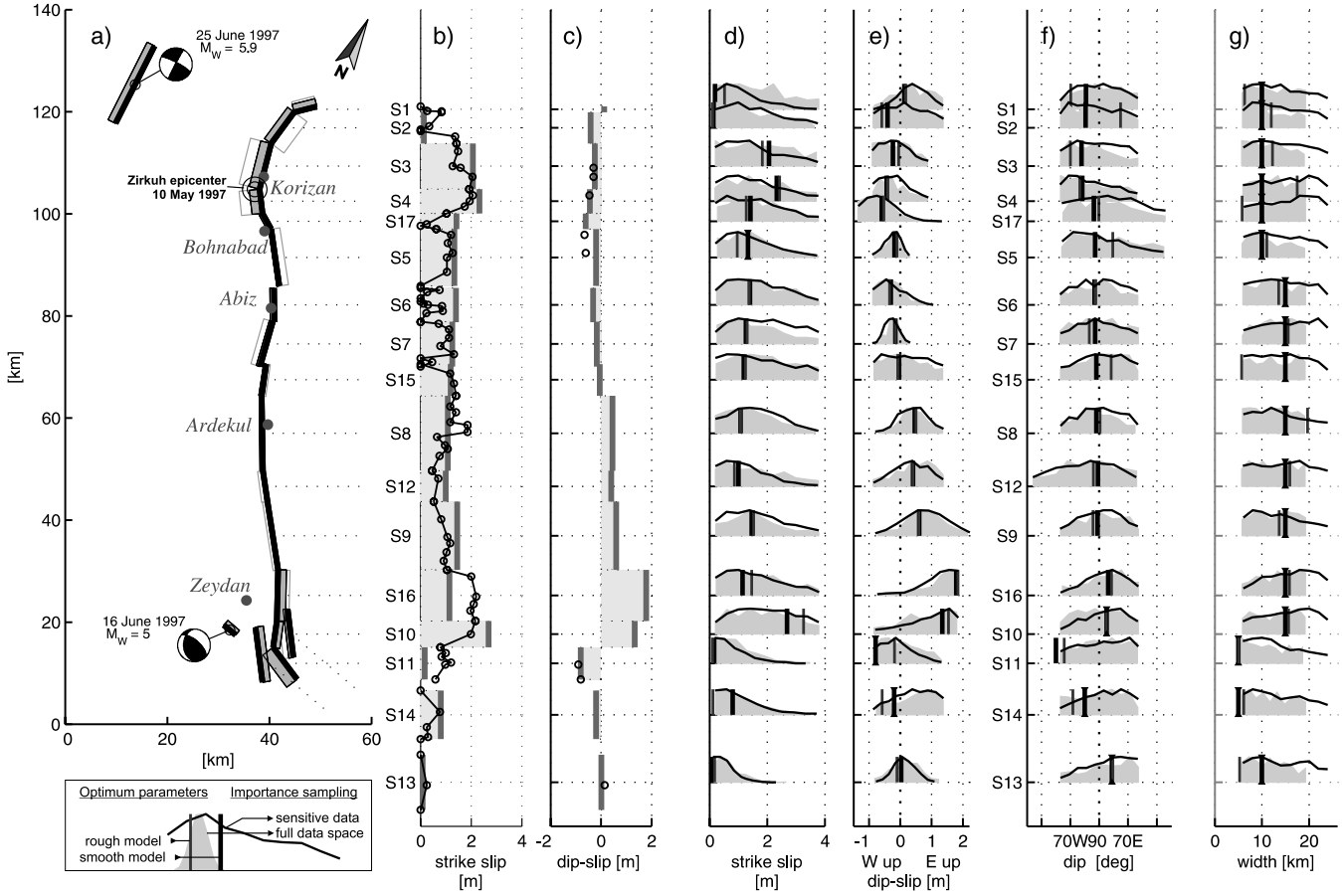

Figure 5. Multisegment model of the Zirkuh earthquake. (a) Map showing the surface projection of segments of two Zirkuh fault models, before (open grey rectangles) and after (grey-filled rectangles) including smoothening of fault-dip between neighbouring segments. Thick lines mark the upper edges of the segments at the surface that are based on the mapped fault surface trace reported by Berberian *et al.* (1999). Two aftershocks are shown as well. (b, c) Optimum strike-slip and dip-slip, respectively, on each fault segment along the main fault in comparison to measured horizontal offsets in the field (black circles). (d–g) Distribution of strike-slip, dip-slip, fault dip and fault width parameters, respectively, from importance sampling using the full data set (shaded areas) and using data subsets (black curves) in comparison to the optimum parameter values (thick vertical lines). The thin vertical lines in (d–g) indicate the parameter values estimated before smoothening fault-segment dip values.

to 2 m between the towns Abiz and Ardekul. From the northern part of the fault to Abiz the modelled dip-slip component shows a slight thrust of some tens of centimetres (west over east) and the fault dip here is mainly between 85° and 70° to the west (Figs 5d–f). Around Ardekul, the fault dip is subvertical and the sense of dip-slip changes signs (east over west), showing around half a metre thrust faulting. The strike-slip displacement picks up again around 20 km south of Ardekul and reaches its maximum of 2.5 m. In this region, the main fault-segment dips become shallower towards the east and the dip-slip reaches almost 2 m. The optimum fault-segment width is highly variable along the fault (Fig. 5g) and seems to be a bit smaller in the northern part of the fault with around 10 km than in the centre and the south with around 15 km. In summary, this first multi-segment model of the Zirkuh earthquake in general agrees well with the amount of strike-slip and the tendency of dip-slip observed in the field (Berberian *et al.* 1999).

We examine the stability of the modelling using the result of the importance sampling (Figs 5d–g) and find in many cases very broad importance sampling distributions, pointing to a rather weak relationship between single model parameters and the overall data misfit as discussed in Section 5.2. The importance sampling distributions often do not decrease significantly towards the parameter limits, more than one high exists in parameter distributions and only dip-slip parameters in the northern and central part of the fault (Fig. 5e) show a confined bell shape.

To get a better idea about how well model parameters of single segments can be resolved we decreased the data space for another set of importance sampling runs, so that the parameter likelihoods were estimated based on segment-specific subsets of the data. We determine the extent of each data subset by the influence model parameters of a single segment can have on the model prediction. Putting extreme fault slip, fault dip and width on one segment only, we select the 'sensitive' data points that show a signal above the noise level. While running importance sampling on these subsets of sensitive data, we keep the full fault model space and vary all fault parameters as before. Therefore, model parameter correlations between neighbouring segments are still reflected in the result (Figs 5d–g). The parameter distributions from segment-wise importance sampling generally look more smooth and are more often Gaussian-shaped than the distributions we obtained from importance sampling in the full data space. While the importance sampling distributions are still broad and therefore only provide a region of high likelihood models, they strongly support the stability of the optimization. Moreover, they give a relative measure of the model parameter uncertainties. We find that dip-slip is generally better constrained than both strike-slip and fault dip. The fault width is poorly constrained along the rupture plane and in some cases the width reaches the lower parameter limit of 5 km. In a parameter correlation analysis (see Supporting Information) we find that in general the fault width is not correlated with other model parameters and therefore does not influence the model stability. Estimated model parameter values also match our pre-defined parameter limits in the southern part of the fault for segments S10-14 and S16. Three of these segments are along the main fault (S16, S10-11) whereas segments S13-14 are subparallel to it (Fig. 5a). As we have no data between these fault strands, poor model resolution and strong model parameter trade-off are to be expected at this location.

We find a clear tendency for fault dip to the west along the northern part of the fault, subvertical dip in the central part, and eastward dipping segments in the south. This variation in fault dip is consistent with what was observed in the field (Berberian *et al.* 1999). However, despite the large-scale agreement, the optimal model has in some cases a considerable fault-dip difference between neighbouring segments, so that the physical concept of a connected rupture plane is not strictly realized in this model. Model segments with low fault slip values predict small surface deformation signals, that is their fault-dip and width constraints are somewhat weaker (e.g. segments S1 and S2) than for segments with stronger fault displacements. This is reflected in the corresponding importance sampling distributions that show no clear fault dip or width preference for these fault segments (Fig. 5a). Another reason for the variability in the modelled fault dip may arise from fault complexities that are not represented in the fault model.

To improve the Zirkuh fault model regarding the fault-dip fluctuations along the main fault, we extend the optimization by constraining the fault-dip difference between neighbouring segments. The aim is to obtain a physically more plausible fault model for the earthquake. In the optimization we add a penalty function e_{dip}, that is based on the sum of fault-dip differences $|d_k - d_{k+1}|$ between neighbouring segments along the main fault (except for segment S11). For M segments the penalty e_{dip} becomes

$$e_{\mathrm{dip}} = \sum_{k=1}^{M-1} |d_k - d_{k+1}| \,. \tag{5}$$

The cost e_{dip} is weighted with respect to the data misfit $\|e_{\mathrm{data}}\|$ (eq. 1) through a weight factor κ_{dip}, so that the total model cost is then

$$e_{\mathrm{total}} = \|e\| + \kappa_{\mathrm{dip}} \cdot e_{\mathrm{dip}}. \tag{6}$$

We choose the weight $\kappa_{\mathrm{dip}} = 0.005$ such that the data misfit $\|e\|$ (eq. 1) still dominates the optimization. In this way, we 'trim' fault-dip values at segments where changes in fault dip do not significantly change the model cost. With inappropriately large values of κ_{dip} on one hand, the data misfit $\|e\|$ will increase again during the optimization, against our intentions. Too small values for κ_{dip} on the other hand will only weakly influence the preference in the model selection for models with small dip variations and it will therefore take longer to reach the optimum model. In addition, we stabilize the fault model in the southern part, where it suffers from model parameter trade-offs, by considering field data from Berberian *et al.* (1999). We use the measured surface offsets at the fault to tighten the limits of the model parameter values in the optimization or even fix them at the segments S10, S11, S13 and S14. Furthermore, we fix the fault width to 10 km in the northern part (segments S1–S4, S17 and S5) and to 15 km for segments south of segment S5 (Fig. 5 and Supporting Information). Because of these additional constraints, the number of free model parameters of the Zirkuh fault is reduced from 68 to 45.

In summary, we reduce the high degree of freedom in our modelling through smoothing the fault dip, fixing the fault width as well as a few other fault parameters in the southern part of the multisegment fault model. Fixing of some parameters in the southern part of the model is necessary because of the strong model parameters correlations that we detected there. By constraining the fault dip of the segments S10, S13 and S14 as well as the dip-slip component on segment S11 and S14 based on field data reported by Berberian *et al.* (1999), we aim for a likely representation of the Zirkuh fault.

The resulting fault model shows more clearly the same general features as seen before (Fig. 5). The westward dipping fault in the north becomes vertical in the central part and easterly dipping in the south. Similarly, the dip-slip changes gradually from the

north towards the south. In most cases the fault-dip now smoothly changes between neighbouring segments, representing a single large connecting fault plane. However, there are still strong fault-dip differences between segments S17 and S5 in the north, S9 and S16 in the southern half of the fault, which may represent real segmentations of the Zirkuh rupture. The last two segments S10 and S11 are affected by the parameter tightening and fixing we applied there, whereas the other two locations might show real segmentations of the Zirkuh rupture.

5.4 Fault slip model

To allow for further model complexity, we subdivide the fault segments into about 2-km-long and 2-km-wide patches in the next modelling step and invert the data for variable slip and rake. We extend the fault length by 4 km and the fault width to 18 km, except for the width of three fault segments (S11, S13 and S14), which are shortened to 6, 10 and 4 km, respectively, to avoid fault intersections at depth.

We assume that slip heterogeneities on the fault have a correlation length that is larger than the 2 km fault patch dimension and therefore implement a smoothing operator D (Du *et al.* 1992; Jónsson *et al.* 2002) into our system of equations using a weighting factor κ:

$$\begin{bmatrix} \mathbf{d}_{\rm obs} \\ \mathbf{0} \end{bmatrix} = \begin{bmatrix} \mathbf{G}_0 \\ \kappa \mathbf{D} \end{bmatrix} \mathbf{m}_0. \qquad (7)$$

Lower κ enables more slip complexity on the fault and improves the data misfit. We choose κ with the help of a trade-off curve (Supporting Information).

We solve eq. (7) using the Fast Non-Negative Least Square (FNNLS) algorithm of Bro & de Jong (1997). The non-negativity constraint allows the rake to vary within only 90° and we thus rotate the local in-plane coordinate axes into the predominant slip direction of the northern and of the southern part of the Zirkuh fault. No smoothing is carried out between these two in-plane rotated coordinate systems. In addition, we force the slip to be equal to zero at 20 km depth.

The main features of the resulting slip model for the Zirkuh earthquake are the same as of the previous multi-segment model (Figs 6 and 5). The fault slip appears to increase from the northern end of the fault plane towards the epicentre near Korizan. Around the epicentre, at depths between 5 and 10 km, the slip exceeds 2 m and has a slightly negative dip-slip (west over east). South of the epicentre the average estimated slip (at 5–10 km depth) is close to 3 m on a 40-km-long section of the fault, from Bohnabad (segment S5) in the north to Ardekul (segment S8) in the south, where the maximum estimated slip reaches almost 4 m. Near Ardekul we also find significant surface slip, whereas the surface slip south of Bohnabad and Abiz (at S5, S6 and S7) is rather small in comparison to the slip below 5 km at these locations. Another region of high strike-slip extends from about 20 km south of Ardekul (segment S9) towards the southern end of the fault where a significant thrust faulting also occurs (segments S16 and S10). The estimated fault rake close to the surface shows almost pure strike-slip north of

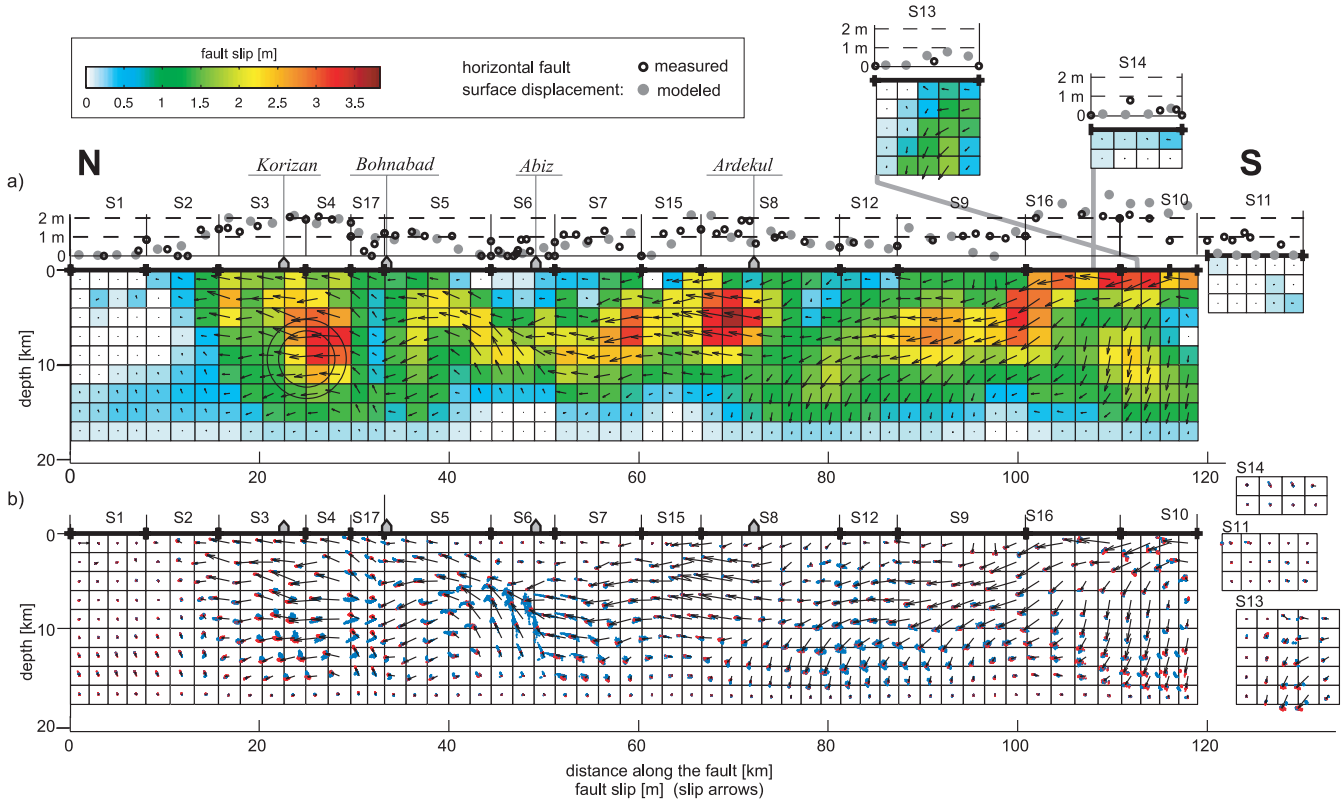

Figure 6. (a) Optimum fault slip model of the Zirkuh earthquake showing the movement of the western side of the fault with respect to the east side. On top of the fault model the horizontal surface slip values, modelled (grey dots) and measured (black circles) by Berberian *et al.* (1999), with distance from the northern end of the fault are given. The large open circle marks the hypocentre location of the Zirkuh earthquake. The segments 11, 13 and 14 are displaced for a better view and the thick lines indicate their correct N–S position. (b) Fault slip variance due to variable fault geometry (small blue dots) and slip variance due to data errors (small red dots) with respect to the optimum model (black arrows).

Ardekul while further south the strike-slip is accompanied with thrust faulting (east over west).

The resulting model predictions of the fault slip model show a good agreement with the measured data and model residuals of the ERS interferograms IG1, IG3 and IG4 are small (Fig. 7). The residuals of the JERS interferogram IG2 are larger than the residuals of the ERS interferograms, because the larger data error in IG2 lead to smaller data weights (Section 5.1).

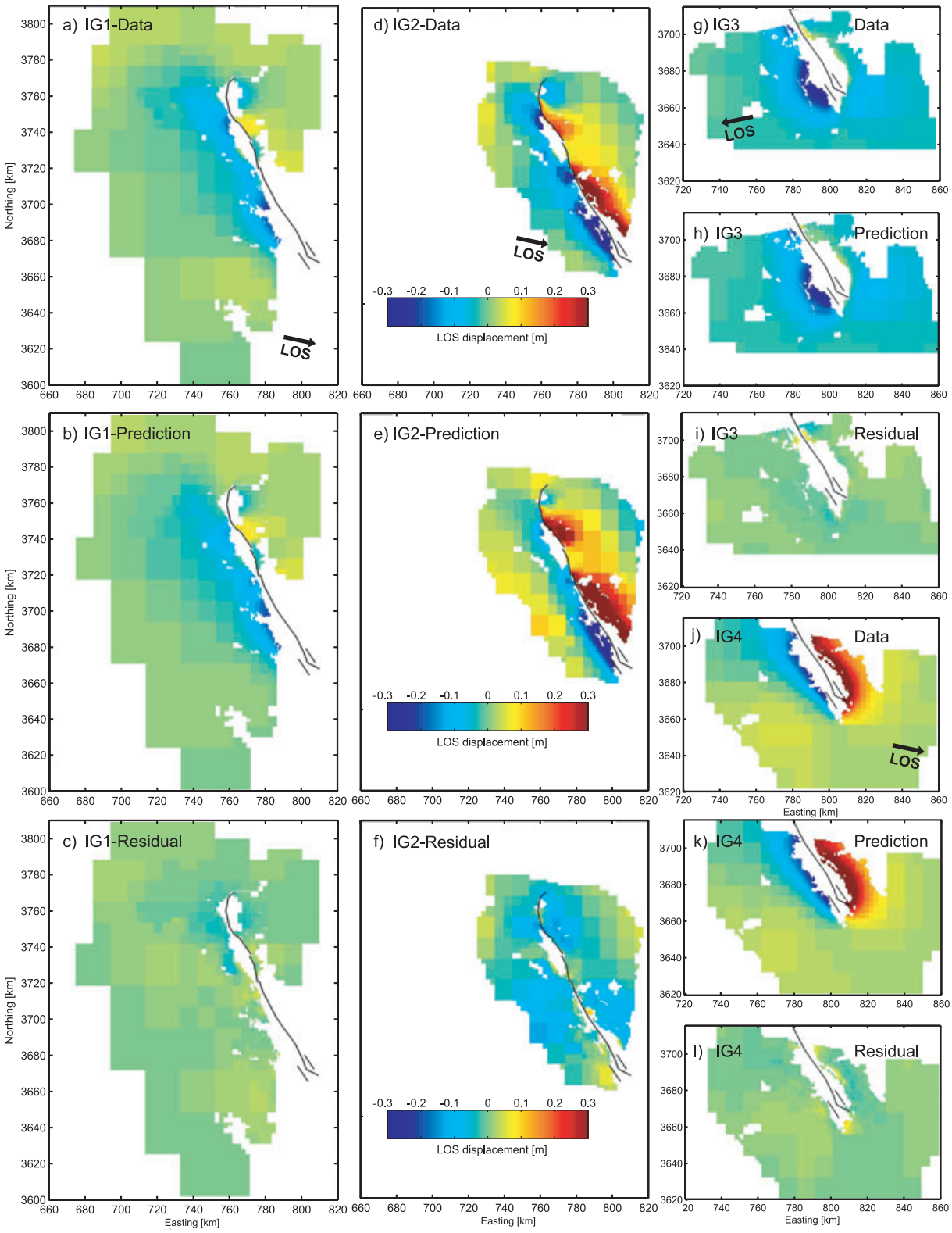

Figure 7. Line-of-sight surface deformation measured with InSAR of IG1-IG4, subsampled (a,d, g and j), the corresponding model predictions of the optimum distributed slip model (b, e, h and k) and model residuals (c, f, i and l). The black line marks the surface trace of the fault model segments.

One way to estimate the uncertainty of the slip model caused by errors in the data, is to perform repeated inversions using many modified data vectors (Wright *et al.* 2003). Multiple sets of synthetic correlated data errors $\varepsilon_{\text{synth}}$ are obtained stochastically from the estimated covariance functions (Table 2), then added to the data vector $\mathbf{d}_{\text{obs}}$ and the result used to invert for a new set of slip model parameters $\mathbf{m}_i$. The distribution of the resulting model parameters at each location on the fault reflects the fault-slip resolution at that location (Fig. 6b). Eq. (7) in this case reads:

$$\begin{bmatrix} \mathbf{d}_{\text{obs}} + \varepsilon_{\text{synth},i} \\ \mathbf{0} \end{bmatrix} = \begin{bmatrix} \mathbf{G}_0 \\ \kappa\mathbf{D} \end{bmatrix} \mathbf{m}_i, \quad i = 1, \ldots, N. \tag{8}$$

We find that the influence of data errors on the fault slip model is not large (Fig. 6b). In general the scatter of fault slip values around the optimum model $\mathbf{m}_0$ is a few tens of centimetres (Fig. 6b), that is relatively small compared with the estimated meter-scale fault slip. The fault slip variations are somewhat stronger in the southern part of the fault, where we expect substantial model parameter correlations. The scatter is also high on subfaults close to Abiz (at the border between segments S6 and S7), where the in-plane coordinate system changes and no smoothing is applied between segments. Therefore, it is probably an artefact due to lack of smoothing.

The uncertainty of the starting-model geometry, described by the Green's function $\mathbf{G}_0$, is not included in eq. (8). To include this uncertainty, we would first need to estimate the error of the uniform-slip model by running thousands of independent and complete non-linear optimizations using noise-modified data vectors (Sudhaus & Jónsson 2009). However, the model complexity and the number of data in this study meant that a single non-linear optimization took several days on a four-processor workstation, which makes the approach of repeated optimizations impractical here.

We expect that model parameter uncertainties are not dominated by the influence of data error, because the signal-to-noise ratio in the ERS interferograms is fairly high. Rather, we think the model parameter uncertainties arise from the model parameter correlations and non-uniqueness of the model. Parameter trade-offs may arise in the north because at this location we have InSAR data from only descending tracks and in the south because of parallel fault planes. Despite we have no quantitative estimate of model-geometry uncertainty, we think an image of the relative sensitivity of the slip model for changes in the fault geometry is instructive. Therefore, we invert the original data $\mathbf{d}_{\text{obs}}$ several times using a set of multisegment model geometries that were sampled in the optimization. In eq. (7), the Green's function describing the optimum model is replaced by a set of $\mathbf{G}_i$:

$$\begin{bmatrix} \mathbf{d}_{\text{obs}} \\ \mathbf{0} \end{bmatrix} = \begin{bmatrix} \mathbf{G}_i \\ \kappa\mathbf{D} \end{bmatrix} \mathbf{m}_i, \quad i = 1, \ldots, N. \tag{9}$$

The criterion for sampling the multisegment models out of the model ensemble from the optimization, or ensemble inference (Sambridge & Mosegaard 2002), is an acceptable data fit. A model from the ensemble is included if its cost is within a cost variance derived from the optimum model cost plus the costs of many synthetic data error realizations.

Slip on subfaults that is strongly affected by the data variance is generally also strongly influenced by the fault geometry variance (Fig. 6b). The influence of the fault geometry variance is usually stronger than that of the data variance. Exceptions are segments S16 and S10, simply because the fault dip is fixed for segments S10, S13 and S14 (Section 5.3, Fig. 5). As mentioned earlier, we decided to fix the dip of these fault segments to stabilize the fault model in the south (Section 5.3). Therefore, the still comparatively high slip variance at segment S10 considering the fixed fault-dip points to an increased uncertainty of the modelled fault slip and the near-vertical rake here might be a biased estimation. Despite these complications in the south the primary features of the fault slip are well resolved for most of the fault model, in particular slip at shallow depths and where fault slip exceeds 2 m.

6 DISCUSSION

Almost no information was available about the subsurface rupture of the Zirkuh earthquake prior to our study. The authors of the only comprehensive study about this event used four point sources to express the large rupture, sources that were constrained using teleseismic observations (Berberian *et al.* 1999). Here we have been able to derive spatial details about subsurface fault slip along the Zirkuh fault, despite incomplete ascending and descending InSAR data coverage and being confronted with an unusually complex source.

Below we discuss the estimated fault-slip characteristics of the Zirkuh earthquake and compare them with the mapped surface fault trace and offset. Further, we discuss the variable fault mechanism along strike and compare it to the seismological findings of Berberian *et al.* (1999). In addition, we look at moment release as a function of depth and compare our results with studies of several other large strike-slip earthquakes.

6.1 Fault slip and geometric complexity

The Abiz fault shows three major step-overs near Bohnabad, at Ardekul, and a few kilometres south of Ardekul (Fig. 1). Furthermore, between Bohnabad and Ardekul the Zirkuh fault trace shows multiple small-scale segments. These fault complexities seem to have influenced the earthquake rupture process. Near the northern end of the Abiz fault, around the Zirkuh hypocentre below Korizan, we find coseismic slip exceeding 1.5 m along a 15 km long portion of the fault. This area of increased slip extends to the surface, where both the mapped and modelled fault offsets reach 2 m (Fig. 6). In 1979, a magnitude 6.6 earthquake took place beneath Korizan. Although it caused smaller surface rupture offsets of about 1 m, it was much more destructive in the Korizan area than the Zirkuh earthquake (Berberian *et al.* 1999). The Zirkuh rupture progressed south across a double bend in the Abiz fault near Bohnabad, unlike the 1979 earthquake, although at this location we find a significant drop in modelled fault slip. This fault kink is a geometric barrier (King & Nábělek 1985) that appears to have stopped the 1979 earthquake. It is associated with a change in fault dip from steep westward to an almost vertical rupture plane (Section 5.3) and small-scale fault complexities that are not represented in our Zirkuh fault model geometry.

South of Bohnabad the estimated fault slip increases again to values around 2 and 3 m. The slip remains high beyond the fault step-over near Ardekul, or for over 40 km (Fig. 6). The surface slip however, is rather low near the middle of this fault section, around the town Abiz, which suffered damage from a magnitude 6 earthquake in 1936 (Berberian *et al.* 1999). The overall maximum fault slip of about 4 m is found directly beneath Ardekul, the town that experienced the worst damage in the Zirkuh earthquake (Berberian *et al.* 1999). Here, the fault step-over seen at the surface seems not to reduce the fault slip at depth.

The southernmost step-over of the Abiz fault is located a few kilometres south of Ardekul and this step-over is associated with

lower slip values (Fig. 6) comparable with the decrease in slip beneath Bohnabad. Further south, the main fault is less segmented than along the northern and the central parts of the fault and in the field the surface trace was found to be confined within a more narrow zone compared to the northern fault parts (Berberian *et al.* 1999). The amount of shallow slip at this location is low, compared to slip at depth (S12 and S9) but further south, in contrast to all other fault segments, large amounts of shallow slip are found (Fig. 6). Here, on the segments S16 and S10, the fault rake begins to deviate from strike-slip and becomes oblique with a significant amount of thrust faulting (east over west).

The ERS interferograms all span 1- to 2-yr-long time periods after the Zirkuh earthquake (Table 1) and therefore probably contain some post-seismic deformation. Unfortunately, the limited ERS SAR data acquisition after the earthquake makes it impossible to separate post-seismic deformation from the coseismic deformation and to study rapidly decaying post-seismic processes (Peltzer *et al.* 1996; Jónsson *et al.* 2003; Fielding *et al.* 2009). The overall good agreement between measured and estimated fault slip near the surface may be explained by either that post-seismic processes after the Zirkuh earthquake did not include significant shallow slip or that the JERS interferogram (IG2) dominates the shallow-slip modelling, despite its low data weight (Sections 4 and 5.1), as its near-field coverage is much better than that of the ERS interferograms. IG2 spans only two months of post-seismic time (Table 1) and therefore should be less affected by post-seismic deformation than the ERS interferograms.

6.2 Zirkuh fault mechanisms from geodetic and seismological estimates

Berberian *et al.* (1999) used both field observations and teleseismic waveform analysis to study the main rupture characteristics of the Zirkuh earthquake, as mentioned earlier. In the latter, they represented the unilateral rupture as four subsequent events with variable focal mechanisms (Fig. 8). To compare our results to their findings, we provide here a more general description of the Zirkuh earthquake on a similar spatial scale as the existing seismological source estimates. We identify three, rather than four, main rupture sections in our fault slip model that are separated by fault step-overs, characterized by low amounts of slip. These sections are the initiating rupture section north of Bohnabad (segments S1–S4 and S17), a central section extending from Bohnabad to Ardekul (segments S5–S8 and S15) and a southern rupture section (Figs 6 and 8). For each rupture section, we provide pseudo-focal mechanisms that we derived from moment-weighted averages of the strike, dip and rake of the fault slip model subfaults (Fig. 6).

We find for the northern rupture section 16 per cent thrust movement (west over east) with respect to strike-slip, and for the central and southern sections 4 per cent (east over west) and 40 per cent

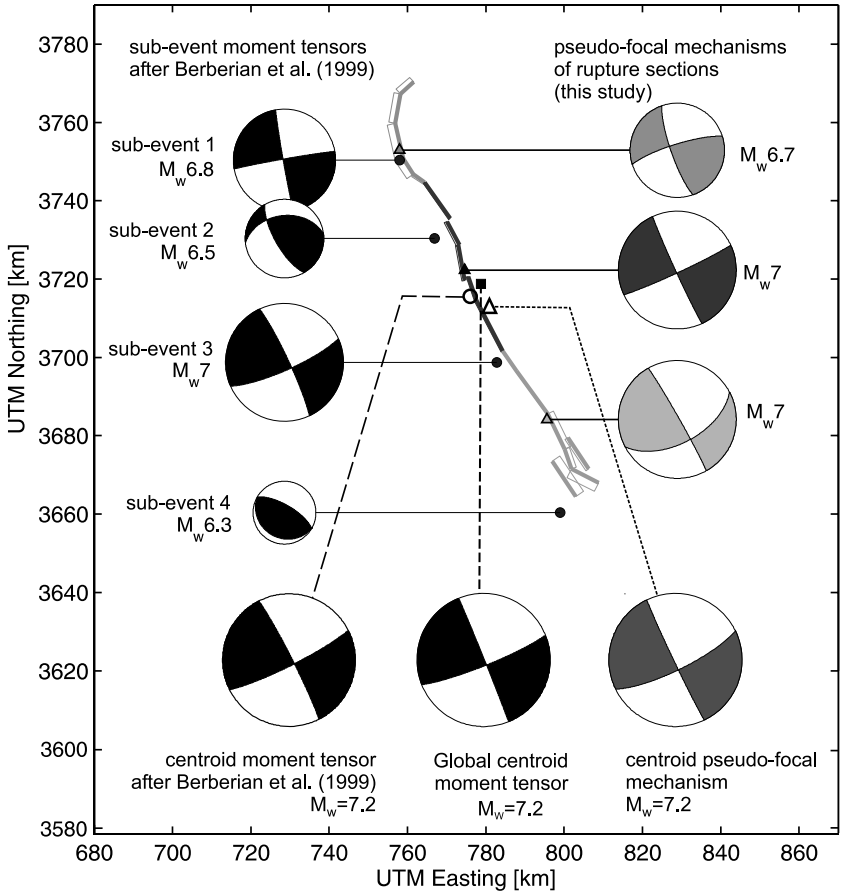

Figure 8. Pseudo-focal mechanisms of the main Zirkuh rupture sections calculated from the fault slip model (Table 3) and sub-event moment tensors after Berberian *et al.* (1999). The fault model segments are shown in a surface projection (thick lines mark upper segment edges) and the different shades of grey indicate the subdivision of the Zirkuh rupture into three sections. The bottom row shows two centroid moment tensor solutions together with the pseudo-focal mechanism representing the entire Zirkuh rupture as estimated in this study (Table 3).

Table 3. Pseudo-focal mechanisms calculated from three main rupture sections of the fault slip model (Figs 6 and 8) and centroid moment tensors for the Zirkuh earthquake (Fig. 8).

	Strike (°)	Dip (°)	Rake (°)	M_0 ($\times 10^{19}$ Nm)	Depth (km)	UTM E[a] (km)	UTM N[a] (km)	Lat (°)	Lon (°)
Section centroids									
North	161	79	169	1.57	6	759.43	3753.12		
Centre	155	88	183	3.12	6	775.88	3722.65		
South	331	87	147	2.85	6	796.79	3684.61		
Centroids									
This study	154	88	192	7.64	6	780.90	3713.63	33.52	60.02
Global CMT	338	90	173	7.70	15	780.31	3719.68	33.58	60.02
Berberian *et al.* (1999)	333	86	173	6.63	15	775.76	3716.04	33.55	59.97

M_0, geodetic or seismic moment, respectively.
[a]UTM zone 40S.

thrust (east over west), respectively (Table 3, Fig. 8). Their corresponding fractional moments from north to south are 18 per cent (M_W 6.7), 42 per cent (M_W 7) and 40 per cent (M_W 7) and add to the total geodetic moment of the Zirkuh earthquake $M_0 = 7.64 \times 10^{19}$ Nm (M_W 7.2). Compared with the seismic focal mechanisms of Berberian *et al.* (1999), our pseudo-focal mechanisms vary less, while showing similar trends (Fig. 8). The seismic focal mechanisms show strong deviations from pure strike-slip only for the two smaller sub-events, whereby in our rupture subdivision we average over larger fault areas with more similar moment release. The variation of the fault mechanisms is therefore less pronounced but persisting in these three rupture sections.

Our estimate of the total geodetic moment is almost identical to the Global Centroid Moment Tensor solution of $M_0 = 7.7 \times 10^{19}$ Nm, but slightly larger than the centroid moment $M_0 = 6.63 \times 10^{19}$ Nm reported by Berberian *et al.* (1999). The centroid mechanisms estimated by Berberian *et al.* (1999), the Global CMT project and this study are similar, with the Global CMT project's solution giving the smallest thrust component, while our estimate shows the strongest (Fig. 8, Table 3).

6.3 Shallow slip deficit on the Zirkuh fault

The Zirkuh fault slip model shows reduced slip near the surface along most of the fault, particularly along the central part of the rupture (Fig. 6). Such shallow slip deficits have been reported in geodetic source models of several large strike-slip earthquakes (Fialko *et al.* 2005). We quantify the slip deficit of the Zirkuh rupture according to Fialko *et al.* (2005) by calculating the average seismic-potency as a function of depth. We analyse the northern, central and southern rupture sections separately, because of their obvious differences in the slip-depth behaviour. In the south of the fault model (S9–S14 and S16) we find no shallow slip deficit (Fig. 9). There is a weak slip deficit in the north that is only significant in the top two rows of the slip model above 4 km depth and it amounts to about 7 per cent (Fig. 9). The slip difference between 3 and 5 km depths (second and third row) is not significant, according to uncertainty estimates of the potency (Fig. 9b). In contrast to the northern and southern sections, the shallow slip deficit along the central part of the rupture is large, also when compared with the Hector Mine and the Izmit earthquakes, and it is similar to what was found for the Landers and the Bam earthquakes. The maximum slip at 7 km depth is the deepest found in this selection of earthquakes and the seismic potency decreases towards the surface to only 40 per cent.

Fialko *et al.* (2005) discuss the nature of the slip deficit focussing on the Bam earthquake. For this earthquake, an extraordinary data quality with very little interferometric phase decorrelation enabled analysis of the surface deformation that strongly supports the existence of shallow fault slip deficit (Fialko *et al.* 2005). The properties of the shallow crust hamper unstable sliding (Tse & Rice 1986) and it seems that distributed inelastic deformation takes place in the volume near the fault rather than on a defined fault surface during co- and post-seismic times (Fialko *et al.* 2005; Fielding *et al.* 2009). Such deformation mechanisms may have acted along the central part of the Zirkuh fault as well.

The ratio of maximum slip at depth and surface slip may depend on the shallow fault and rock properties as well as on the stress state just before and during the rupture (Fialko *et al.* 2005). The weak slip deficit apparent in the north of the Zirkuh fault could then be related to weaker rocks in the fault zone due to the short 18-year interseismic period between the 1979 Korizan earthquake (M_W 6.6) and the Zirkuh earthquake. In the central fault part the rest since the last large earthquake near Abiz and the Zirkuh earthquake lasted 60 years. On the southern rupture section our fault slip model is in a very good agreement with measured fault offsets (Fig. 6). However, an interpretation of the shallow slip excess here is a bit problematic, because of limited near-fault data and faulting on parallel fault strands.

6.4 Modelling of complex segmented faults

Multisegment fault models have been generated for several other large strike-slip earthquakes, for example for the 1999 Izmit (Delouis *et al.* 2002), the Denali (Wright *et al.* 2004) and the Kokoxili (Lasserre *et al.* 2005) earthquakes. In these studies the fault dip was fixed, but was not allowed to vary, like in the Zirkuh fault model estimation. There, independent information on the fault dip as aftershock distributions helped to define a likely fault dip *a priori*.

In two geodetic source studies on the Hector Mine earthquake (Jónsson *et al.* 2002; Simons *et al.* 2002), the fault dip was an explicit free parameter in the modelling and for the 1997 Manyi earthquake (Tibet) Funning *et al.* (2007) showed with testing different fault dips that the data fit improves significantly with fault dip that changes direction along the fault. If there is no reliable independent information on fault dip, simultaneous optimization of fault dip and slip is important to avoid bias in the slip estimates, because fault slip and dip tend to be correlated (Fukahata & Wright 2008; Sudhaus & Jónsson 2009). By smoothing the fault-dip values along strike, we avoid problematic jumps in the fault dip on the segmented model fault plane. At the same time, the fault-dip smoothing stabilizes the optimization by reducing the degrees of freedom in the parameter space.

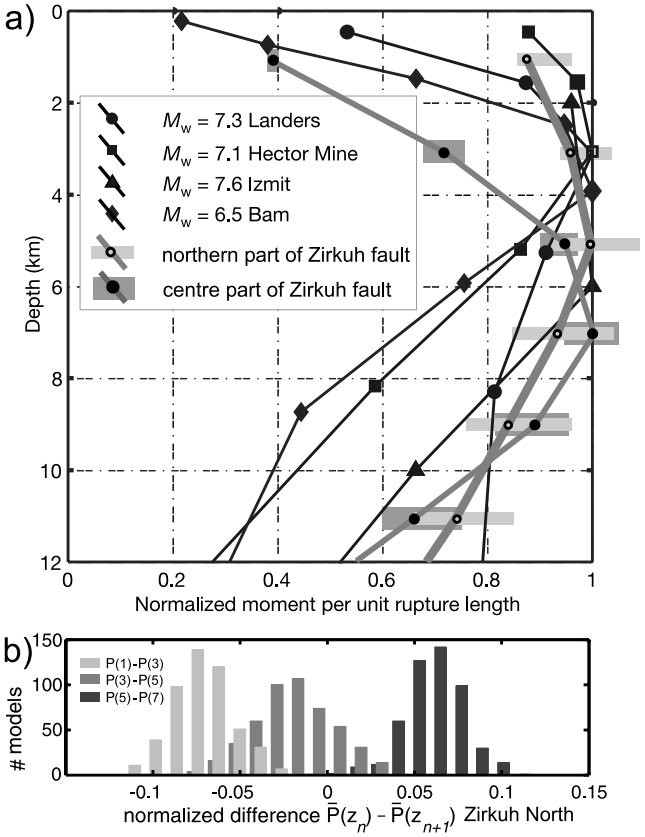

Figure 9. (a) Seismic potency P, the integral of coseismic slip along the rupture, normalized and as a function of depth z: $\bar{P}(z) = \int_0^L P(x,z)\mathrm{d}x / \max(\int_0^L P(x,z)\mathrm{d}x)$ for several large strike-slip earthquakes after Fialko *et al.* (2005): the Landers (Fialko 2004), the Hector Mine (Simons *et al.* 2002), the Izmit (Cakir *et al.* 2003) and the Bam (Fialko *et al.* 2005) earthquakes together with $\bar{P}(z)$ of the northern Zirkuh rupture section (segments S2–S4 and S17) and the central rupture section (segments S5–S8 and S15). Grey horizontal bars mark 95 per cent confidence estimates of $\bar{P}(z)$ derived from the distributed slip model ensemble in Fig. 6b. (b) Histograms showing the differences between average seismic potencies $\bar{P}(z_i)$ at different depths z_i on the northern Zirkuh rupture section (segments S2–S4 and S17) considering the ensemble of Zirkuh fault slip models (Fig. 6b). The three histograms illustrate the differences $\bar{P}(z_i) - \bar{P}(z_{i+1})$ for $z =$ (1, 3, 5, 7) km and $i = (1, 2, 3)$.

7 CONCLUSIONS

We presented a detailed fault slip model of the 1997 Zirkuh earthquake with multiple segments that we determined using InSAR data from ERS (C-band) and JERS (L-band) satellites. The combination of C- and L-band InSAR images leads to almost complete coverage of the far-field and the near-field surface deformation measurements of the Zirkuh earthquake, which helped to constrain the complex fault geometry. We optimized the multisegment fault model using an evolutionary algorithm and evaluated the optimum fault model from importance sampling distributions. To account for the fault complexity of the Zirkuh fault, we included the fault dip as a free model parameter in the source modelling and introduced fault-dip smoothing between neighbouring fault segments to reduce large shifts in fault dip along the fault plane. The resulting model fault plane has a westerly dip along the northern part of the fault, is subvertical in the centre, and gradually changes to an easterly tilted plane in the south. In these three rupture sections, the fault mechanism changes from slight thrust (west over east) in the north to almost pure strike-slip in the centre and significant thrust (east over west) in the south. These findings are consistent with subevent fault mechanisms of the Zirkuh earthquake that were deduced from teleseismic data (Berberian *et al.* 1999).

The heterogeneous fault slip of the Zirkuh model has locally more than 2 m of shallow slip and is along the entire fault in a good agreement with the measured fault offsets at the surface (Berberian *et al.* 1999). Below 2 km the fault slip is generally larger varying between 1 m and more than 3 m. The maximum slip of almost 4 m is found beneath Ardekul, the town that sustained the greatest amount of damage during the Zirkuh earthquake (Berberian *et al.* 1999). Low slip regions on the fault plane coincide with two large fault step-overs of the Abiz fault, which suggests that the fault geometry influenced the amount of coseismic fault slip.

The Zirkuh fault slip model has a shallow slip deficit along the fault that is comparable with other large strike-slip earthquakes (Fialko *et al.* 2005), but the deficit is weaker in the north than along the central part of the fault. This along-strike variation in shallow slip deficit possibly results from different rock properties related to different interseismic times of only 18 years in the north and 60 years in the central part of the fault.

ACKNOWLEDGMENTS

We thank Eric Fielding for sharing information about the Zirkuh earthquake and his support in the early days of this study as well as Amir Farahbod for providing the Zirkuh aftershock data. Damiano Monelli supported the implementation of the importance sampling. Further, we like to thank Max Werner and Martin Mai for fruitful discussions on the behaviour of the importance sampling in this special case and Domenico Giardini for discussions. Also, we thank Rowena Lohman and an anonymous reviewer for their careful reading and their useful comments on the paper that helped to clarify its content. The ERS SAR data were provided by ESA through Category-1 project #3639.

REFERENCES

Berberian, M. & King, G.C.P., 1981. Towards a paleogeography and tectonic evolution of Iran, *Can. J. Earth Sci.,* **18,** 210–265.

Berberian, M., Jackson, J.A., Qorashi, M., Khatib, M.M., Priestley, K., Talebian, M. & Ghafuri-Ashtiani, M., 1999. The 1997 May 10 Zirkuh (Qa'enat) earthquake (Mw 7.2): faulting along the Sistan suture zone of eastern Iran, *Geophys. J. Int.,* **136,** 671–694.

Beyer, H.-G., 2001. The theory of evolution strategies, in *Natural Computing,* ed. Rozenberg, G., Springer Verlag, Heidelberg.

Bro, R. & Jong, S.D., 1997. A fast non-negativity-constrained least squares algorithm, *J. Chemometr.,* **11,** 393–401.

Cakir, Z., de Chabalier, J.-B., Armijo, R., Meyer, B., Barka, A. & Peltzer, G., 2003. Coseismic and early post-seismic slip associated with the 1999 Izmit earthquake (Turkey), from SAR interferometry and tectonic field observations, *Geophys. J. Int.,* **155**(1), 93–110.

Chen, C.W. & Zebker, H.A., 2001. Two-dimensional phase unwrapping with use of statistical models for cost functions in nonlinear optimization, *J. Opt. Soc. Am. A,* **18**(2), 338–351.

Chilés, J.-P. & Delfiner, P., 1999. Geostatistics—modelling spatial uncertainties, *Wiley Series in Probability and Statistics. Applied Probability and Statistics Section,* John Wiley & Sons. Inc., New York, NY.

Delouis, D., Giardini, D., Lundgren, P. & Salichon, J., 2002. Joint inversion of InSAR, GPS, teleseismic, and strong-motion data for the spatial and temporal distribution of earthquake slip: application to the 1999 I'zmit mainshock, *Bull. seism. Soc. Am.,* **92**(1), 278–299.

Du, Y.-J., Aydin, A. & Segall, P., 1992. Comparison of various inversion techniques as applied to the determination of a geophysical deformation

model for the 1983 Borah Peak earthquake, *Bull. seism. Soc. Am.,* **82**(4), 1840–1866.

Dziewonski, A.M., Chou, T.-A. & Woodhouse, J.H., 1981. Determination of earthquake source parameters from waveform data for studies of global and regional seismicity, *J. geophys. Res.,* **86,** 2825–2852.

Farahbod, M.A., Lindholm, C., Mokhtari, M. & Bungum, H., 2003. Aftershock analysis for the 1997 Ghaen-Birjand (Ardekul) earthquake, *JSEE,* **5**(2), 1–10.

Farr, T.G. *et al.*, 2007. The shuttle radar topography mission, *Rev. Geophys.,* **45,** doi: 10.1029/2005RG000183.

Fialko, Y., 2004. Evidence of fluid-filled upper crust from observations of post-seismic deformation due to the 1992 Mw 7.3 Landers earthquake, *J. geophys. Res.,* **109,** doi:10.1029/2004JB002985.

Fialko, Y., Sandwell, D., Simons, M. & Rosen, P.A., 2005. Three-dimensional deformation caused by the Bam, Iran, earthquake and the origin of shallow slip deficit, *Nature,* **435,** doi:10.1038/nature03425.

Fielding, E.J., Jackson, J.A. & Berberian, M., 2000. Complex deformation in eastern Iran: implications from SAR interferometric analysis of the 10 May 1997 Zirkuh $M_w = 7.2$ earthquake, *EOS, Trans. Am. geophys. Un.,* **81**(48), Fall Meet. Suppl. Abstract T72B-08.

Fielding, E., Lundgren, P., Bürgmann, R. & Funning, G.J., 2009. Shallow fault-zone dilatancy recovery after the 2003 Bam earthquake in Iran, *Nature,* **458**(7234), 64–68.

Fukahata, Y. & Wright, T.J., 2008. A non-linear geodetic data inversion using ABIC for slip distribution on a fault with an unknown dip angle, *Geophys. J. Int.,* **173,** 353–364.

Funning, G.J., Parsons, B. & Wright, T.J., 2007. Fault slip in the 1997 Manyi, Tibet earthquake from linear elastic modelling of InSAR displacements, *Geophys. J. Int.,* **169**(3), 988–1008.

Gershenfeld, N., 1999. *The Nature of Mathematical Modeling,* Cambridge University Press, New York.

Goldstein, R.M. & Werner, C.L., 1998. Radar interferogram filtering for geophysical applications, *Geophys. Res. Lett.,* **25**(21), 4035–4038.

Grünthal, G., Bosse, C., Sellami, S., Mayer-Rosa, D. & Giardini, D., 1999. Compilation of the GSHAP regional seismic hazard for Europe, Africa and the Middle East, *Annali di Geofisica,* **42**(6), 1215–1223.

Hanssen, R., 2001. Radar Interferometry, data interpretation and error analysis, in *Remote Sensing and Digital Image Processing,* Vol. 2, Kluwer Academic Publishing, Dordrecht.

Jónsson, S., Zebker, H.A., Segall, P. & Amelung, F., 2002. Fault slip distribution of the 1999 Mw7.2 Hector Mine earthquake, California, estimated from satellite radar and GPS measurements, *Bull. Seism. Soc. Am.,* **92**(4), 1377–1389.

Jónsson, S., Segall, P., Pedersen, R. & Björnsson, G., 2003. Post-earthquake ground movements correlated to pore-pressure transients, *Nature,* **424,** 179–183.

King, G. & Nábělek, J., 1985. Role of fault bends in the initiation and termination of earthquake rupture, *Science,* **228**(4702), 984–987.

Knospe, S.H.-G. & Jónsson, S., 2010. Covariance estimation for dInSAR Surface deformation measurements in presence of anisotropic atmospheric noise, *IEEE Trans. Geosci. Remote Sensing,* **48**(4), 2057–2065.

Mai, P.M. & Beroza, G.C., 2000. Source scaling properties from finite-fault-rupture models, *Bull. seism. Soc. Am.,* **90**(3), 604–615.

Lasserre, C., Peltzer, G., Crampé, F., Klinger, Y., Woerd, J.V.D. & Tapponnier, P., 2005. Coseismic deformation of the 2001 $Mw = 7.8$ Kokoxili earthquake in Tibet, measured by synthetic aperture radar interferometry, *J. geophys. Res.,* **110**(B12), doi:10.1029/2004JB003500.

Lohman, R.B. & Simons, M., 2001. The May 10, 1997 Ardekul (Zirkuh) earthquake in Iran: crustal deformation constrained by Interferometric Synthetic Aperture Radar and inversions for fault slip, geometry, and elastic parameters, *EOS, Trans. AGU Fall Meet. Suppl.,* **82**(47), Abstract G31B-0147.

Monelli, D. & Mai, P.M., 2008. Bayesian inference of kinematic earthquake rupture parameters through fitting of strong motion data, *Geophys. J. Int.,* **173**(1), 220–232.

Monelli, D., Mai, P.M., Jónsson, S. & Giardini, D., 2009. Bayesian imaging of the 2000 Western Tottori (Japan) earthquake through fitting of strong motion and GPS data, *Geophys. J. Int.,* **176**(1), 135–150.

Okada, Y., 1985. Surface deformation due to shear and tensile faults in a half-space, *Bull. seism. Soc. Am.,* **75**(4), 1135–1154.

Peltzer, G., Rosen, P., Rogez, F. & Hudnut, K., 1996. Postseismic rebound in fault step-overs caused by pore fluid flow, *Science,* **273,** 1202–1204.

Peyret, M., Cadoul, B. & Chéry, J., 2004. Measuring co-seismic deformation of the Fandoqa (14/03/98 - Mw 6.6) and Zirkuh (10/05/97 - Mw 7.1) earthquakes, SE Iran, in *Proceedings to the FRINGE 2003 Workshop*, Frascati.

Sambridge, M. & Mosegaard, K., 2002. Monte Carlo methods in geophysical inverse problems, *Rev. Geophys.,* **40**(3), doi: 10.1029/2000RG000089.

Scharroo, R., Visser, P.N.A.M. & Mets, G.J., 1998. Precise orbit determination and gravity field improvement for the ERS satellites, *J. geophys. Res.,* **103**(C4), 8113–8127.

Smith, M.L., Scales, J.A. & Fischer, T.L., 1992. Global search and genetic algorithms, *Geophysics,* **11**(1), 22–26.

Simons, M., Fialko, Y. & Rivera, L., 2002. Coseismic deformation from the 1999 Mw 7.1 Hector Mine, California, earthquake as inferred from InSAR and GPS observations, *Bull. seism. Soc. Am.,* **92**(4), 1390–1402.

Sudhaus, H. & Jónsson, S., 2009. Improved source modelling through combined use of InSAR and GPS under consideration of correlated data errors: Application to the June 2000 Kleifarvatn earthquake, Iceland, *Geophys. J. Int.,* **176**(2), 389–404.

Tarantola, A., 2005. *Inverse Problem Theory and Methods for Model Parameter Estimation,* Society for Industrial and Applied Mathematics, Philadelphia, PA.

Tse, S.T. & Rice, J.R., 1986. Crustal earthquake instability in relation to the depth variation of frictional slip properties, *J. geophys. Res.,* **91**(B9), 9452–9472.

Vernant, P. *et al.*, 2004. Present-day crustal deformation and plate kinematics in the Middle East constrained by GPS measurements in Iran and northern Oman, *Geophys. J. Int.,* **157**(1), 381–389.

Walker, R.T. & Khatib, M.M., 2006. Active faulting in the Birjand region of NE Iran, *Tectonics,* **25**(4), doi:10.1029/2005TC001871.

Werner, C.L., Wegmmüller, U., Strozzi, T. & Wiesmann, A., 2000. Gamma SAR and interferometric processing software, in *Proceedings of the ERS-Envisat Symposium*, Gothenburg.

Wright, T.J., Lu, Z. & Wicks, C., 2003. Source model for the Mw 6.7, 23 October 2002, Nenana Mountain Earthquake (Alaska) from InSAR, *Geophys. Res. Lett.,* **30**(18), doi:10.1029/2003GL018014.

Wright, T.J., Lu, Z. & Wicks, C., 2004. Constraining the slip distribution and fault geometry of the Mw 7.9, 3 November 2002, Denali fault earthquake with interferometric synthetic aperture radar and global positioning system data, *Bull. seism. Soc. Am.,* **94**(6B), S175–S189.

APPENDIX A: OVERLAPPING-DATA WEIGHT FACTOR

Our combined InSAR data set has a heterogeneous spatial coverage. There are areas near the southern part of the Zirkuh fault that are covered by all four InSAR data sets, whereas in the north only up to two data sets cover the same area (Fig. A1a). Therefore, the coseismic deformation is in some areas better observed through multiple observations than in other areas. Up to this point, our weighting has been based on the data covariance (Section 5.1). Hence, when combining M different data sets that all cover the same area, the effective weight of that area is approximately the average point weight times M. Such a large weight increase can only be justified when the combined data sets are linearly independent, which for InSAR data is usually not the case.

We account for overlapping data coverage by introducing an additional weighting factor for each point on the ground. The *overlapping-data weight factor* varies with location, as the number M of overlapping data sets is different from one area to another and as the LOS vectors also vary with location. In the general case,

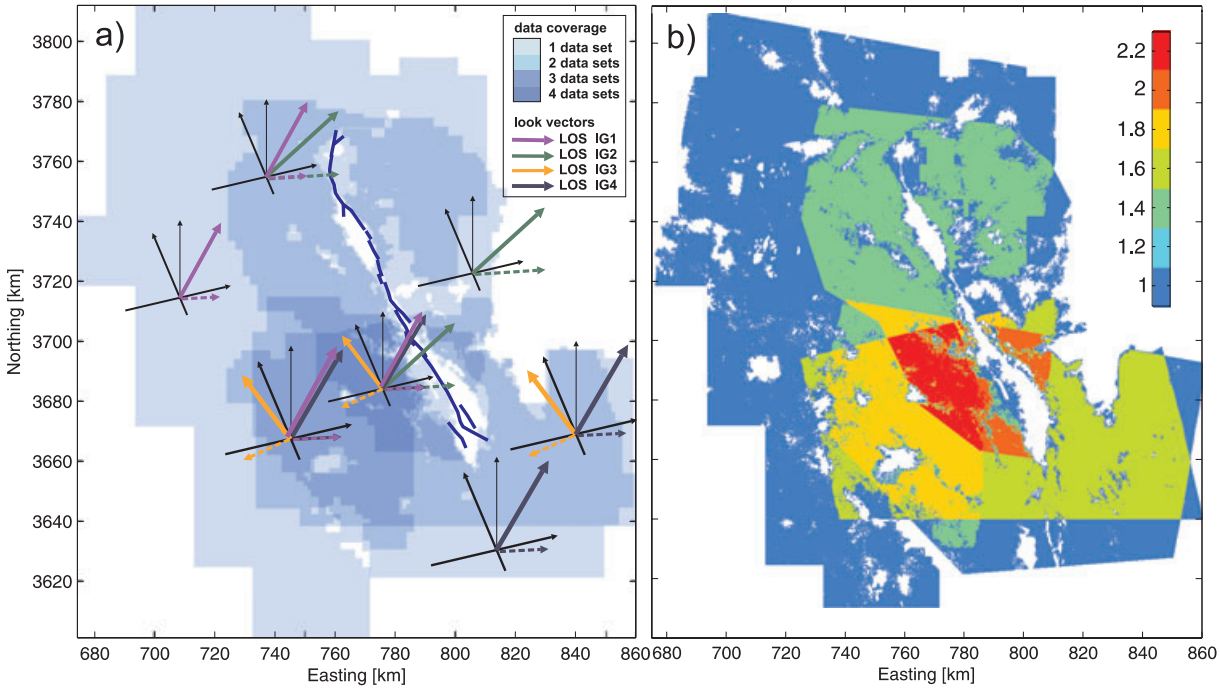

Figure A1. (a) Data coverage overlap for interferograms IG1-IG4 and the corresponding 3-D LOS vectors pointing from the ground towards the satellite (solid arrows) with their surface projections (dashed arrows). (b) Overlapping-data weights of pixels in the study area.

where we have M overlapping observations at a single location, we have M different LOS vectors that are neither orthogonal nor parallel to one another. For each location we collect the corresponding M LOS vectors and store them, line by line, in matrix $\mathbf{U}$:

$$\mathbf{U}^{\mathbf{T}} = [\mathbf{u}_1, \mathbf{u}_2, \ldots, \mathbf{u}_M]. \tag{A1}$$

Then the matrix

$$\mathbf{V} = \mathbf{U} \cdot \mathbf{U}^{\mathbf{T}} \tag{A2}$$

is a symmetric $M \times M$ matrix that provides the scalar product between all the LOS vectors at that given location. The sum of the columns (or lines) of matrix $\mathbf{V}$: $\mathbf{v} = \sum_{j=1}^{M} |\mathbf{V}_{ij}|$ provides information about the linear dependency between the data sets. For example, $v_1 = \sum_{j=1}^{M} |\mathbf{V}_{1j}| = M$ if all LOS vectors in $\mathbf{U}$ are parallel to $\mathbf{u}_1$, whereas $v_1 = \sum_{j=1}^{M} |\mathbf{V}_{1j}| = 1$ if $\mathbf{u}_1$ is orthogonal to the other LOS vectors.

The overlapping-data weight factor w_i for the ith data set is defined as

$$w_i = \frac{1}{\sqrt{\sum_{j=1}^{M} |\mathbf{V}_{ij}|}}, \tag{A3}$$

so that linearly dependent data points are down-weighted by a factor $w_i < 1$ and an observation that is linearly independent from the other data sets would keep an unchanged weight, that is $w_i = 1$. However, the overlapping-data weight factors for M similar LOS vectors are always larger than $1/M$. The weight of a given location on the ground is the sum $W = \sum_{i=1}^{M} w_i$ which better reflects the measurement improvement of the deformation through multiple observations.

In our Zirkuh example, we have at most four data sets covering the same area. Without the additional weighting introduced above the weight would equal the number of overlapping data sets, that is 1, 2, 3, or 4. However, due to the linear dependency of the observations, the overlapping-data weight factor of pixels covered by four data sets is only about 2.2 (Fig. A1b). Therefore, the overlapping-data weight factor depends on the number of overlapping observations as well as how diverse the corresponding LOS vectors are. For example, in areas where IG1 and IG2 overlap the additional weight factor is lower than where IG3 and IG4 are combined, because in the latter case the observations are less linearly dependent (Fig. A1b).

SUPPORTING INFORMATION

Additional Supporting Information may be found in the online version of this article:

Figure S1. Unwrapped interferograms from ERS-1/2 (C-band) and JERS-1 (L-band) satellite data (Table 1) in foreground of shaded topography in UTM coordinates (UTM zone 40S).
Figure S2. Model parameter correlation coefficients calculated from importance sampling model ensemble.
Table S3. Fault parameters of the multi-segment model with freely variable dip ('rgh') and the final smoothed model ('sm'). Stars mark the parameters that we kept fixed, and double stars where we put tight parameter bounds.
Figure S4. Data misfit as a function of model solution roughness with the chosen weighting factor indicated with a large cross.

Please note: Wiley-Blackwell is not responsible for the content or functionality of any supporting materials supplied by the authors. Any queries (other than missing material) should be directed to the corresponding author for the article.